Journal of Physics: Conference Series **506** (2014) 012013 doi:10.1088/1742-6596/506/1/012013

Characterization of the shear layer in a Mach 3 shock/turbulent boundary layer interaction

C Helm[1], M P Martin[1] and P Dupont[2]

[1] Department of Aerospace Engineering, University of Maryland, College Park, MD, 20742
[2] Institut Universitaire des Systèmes Thermiques et Industriels, UMR 7343 CNRS. Aix–Marseille Université, Marseille, France.

E-mail: pmartin@umiacs.umd.edu

Abstract. A detailed characterization of the shear layer in a direct numerical simulation of a Mach 3, separated shock/turbulent boundary layer interaction over a 24^o compression ramp is presented. Similarity solutions are identified in the time-averaged shear layer and the growth of the shear layer is found to be approximately linear. In addition to the time averaged spatial organization of the shear layer, the characteristic frequencies and time scales of the large Kelvin–Helmholtz vortices are determined and are found to be consistent with the energized frequency content in the pre-multiplied power spectra of the wall pressure. The three-dimensional nature of the mixing layer vortices are identified using two-dimensional correlation contour plots and a technique for the identification of individual vortices. The large vortices shed from the separated region are found to lie in a plane parallel to the ramp surface, but angled at $\pm 45^o$ to the freestream direction.

1. Introduction

The shock/turbulent boundary layer interaction (STBLI) is an almost unavoidable phenomena in many compressible flow applications such as transonic airfoils, supersonic engine inlets, scramjet isolators, rocket nozzles and so forth. Strong STBLIs pose a significant problem in engineering applications because they are characterized by a low-frequency unsteadiness (two orders of magnitude lower than the turbulence motions of the incoming boundary layer) where the shock experiences large amplitude excursions from its mean position, causing potentially destructive fluctuations in temperature and pressure on the vehicle surface [1-4]. A thorough understanding of the dynamics of the STBLI will help in the development of more accurate predictive models for design applications and possible control solutions. Although the dynamics of separated STBLIs have been studied extensively [1,5-14], the overall understanding is still limited to only a general description of the statistical behaviour of the low-frequency cycle and statistical links between observed phenomena within the interaction. Models for the unsteadiness have been proposed in the past, however, an explicit explanation of the driving mechanism for the low-frequency shock motion has not yet been discovered and much work is still needed in this area of research.

In this paper the focus is on the behaviour and characterization of the shear layer that forms downstream of the shock and above the region of separation. Previous research has provided reason to believe that the shear layer plays a significant role in dictating the overall dynamics of the interaction. For example, Piponniau, Dussauge, Debieve, and Dupont [10] proposed a model of the low-frequency cycle by assuming that the depletion of the separation bubble is a result of

Content from this work may be used under the terms of the Creative Commons Attribution 3.0 licence. Any further distribution of this work must maintain attribution to the author(s) and the title of the work, journal citation and DOI.
Published under licence by IOP Publishing Ltd

Table 1: Characteristics of the incoming boundary layer.

M	Re_θ	δ^+	$U_{\inf}$ (ms^{-1})	δ (mm)	δ^* (mm)	θ (mm)	H
2.91	2.9×10^3	3.4×10^2	610	7.1	2.58	0.47	5.49

fluid entrainment by the shear layer, and the authors were able to obtain a reasonable estimate of the low-frequency of their reflected shock interaction from experimental PIV data. Also, large vortical structures associated with the Kelvin-Helmholtz type instability are known to exist in both the reflected shock configuration (Dupont, Piponniau, Sidorenko, and Debieve [15] and Souverein *et al* [13]), and the compression ramp configuration (Priebe & Martin [14]). Agostini *et al* [16] used cross-correlations between the streamwise position of the shock and the pressure field in their large-eddy simulations of reflected shock interactions to provide further evidence that large, periodic vortices are generated in the shear layer and convect downstream. Priebe & Martin [14] observed a sawtooth-like motion of the reattachment point of the separation bubble in their direct numerical simulation of a Mach 3 compression ramp and, basing their conclusions on observations of similar behaviour in incompressible separation bubbles (Kiya & Sasaki [17]), associated this motion with the passage of these large vortical structures into the downstream flow.

To lend more insight into the behaviour of the shear layer and how it might contribute to the low-frequency unsteadiness of STBLI flows, a detailed characterization of the shear layer in the DNS of a Mach 3 STBLI over a 24^o compression ramp is presented here. The paper is organized as follows. The DNS data set is introduced in section 2. In section 3, the time-averaged spatial description of the shear layer is presented, and in section 4 the timescales and spatial organization of the shear layer vortices are described. A summary of conclusions is given in section 5.

2. Flow and computational method

The analytical results presented in this paper were produced using data from a direct numerical simulation (DNS) of a shock-turbulent boundary layer interaction (STBLI) where the shock is produced by a 24^o compression ramp. The incoming boundary layer is fully developed with a freestream Mach number of 2.9. This particular data set has been very well documented in the paper by Priebe & Martin [14] and the reader is referred to this paper for a complete description of the computational methods used and of the time-averaged and instantaneous organization of the flow, as well as a thorough analysis of frequency content and spectra. In summary, upstream of the shock the freestream velocity and temperature are $U_{\inf} = 610\mathrm{m/s}$ and $T_{\inf} = 107\mathrm{K}$. The incoming boundary thickness is $\delta = 7.1\mathrm{mm}$ and the Reynolds number based on the momentum thickness is $Re_\theta = 2900$. A list of the important parameters of the incoming turbulent boundary layer are provided in Table 1. The interaction is fully separated in the time-averaged sense and the separation length defined as the distance along the wall between the mean separation point and the mean reattachment point is $L_{\mathrm{sep}} = 3.0\delta$. The computational grid is curvilinear with a resolution of $1024 \times 160 \times 128$ grid points in the streamwise, spanwise and wall-normal directions respectively. This corresponds to a physical domain size of approximately $(13.7 \times 2.0 \times 4.4)\delta$. The inflow conditions were prescribed from a separate auxiliary DNS of a spatially developing, flat-plate, turbulent boundary layer. The auxiliary DNS was computed on a Cartesian grid of size $410 \times 160 \times 112$ points with physical dimensions $(8.3 \times 2.0 \times 8.2)\delta$. The same computational

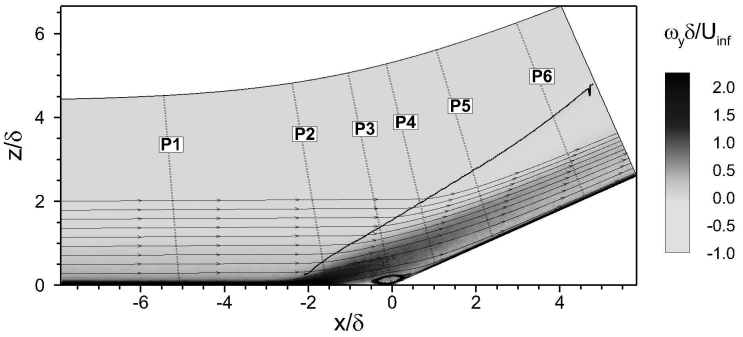

Figure 1: Compression ramp mean-flow organization.

method and boundary conditions as were used for the ramp simulation were used for the auxiliary DNS except that the inflow conditions were assigned using the recycling/rescaling method of Xu & Martin [18].

The three-dimensional space of the ramp domain is expressed in terms of the standard x, y, and z coordinate axes where x is in the streamwise direction with respect to the incoming flow, y is in the spanwise direction, and z is perpendicular to the wall surface ahead of the ramp. The velocity components in the three respective directions are indicated by u, v, and w.

The time- and spanwise-averaged organization of the ramp flow is shown in Figure 1. The average location of the shock is visualized in Figure 1 by the vertical location of maximum $|\nabla P|$ as a function of x. The boundary layer and the shear layer just downstream of the shock are visualized by the increased levels of the in-plane vorticity ω_y. Mean streamlines clearly demonstrate a region of recirculation at the ramp corner. In the DNS computational domain there are six yz grid planes from which time signals of the primitive flow variables are output at a high-frequency sample rate and the locations of these planes are indicated in Figure 1. The high frequency time signals are output at the sampling rate $f_s = 200U_{inf}/\delta$ for a duration of $766\delta/U_{inf}$.

3. Time-averaged shear layer

The mean shear layer in the DNS data is visualized in Figure 2 by the contour plot of the averaged two-dimensional turbulent kinetic energy or TKE. In this section, an average quantity refers to an averaging in both time and the spanwise direction. The mean separation point is $x_s/\delta = -2.1$ and the mean reattachment point is $x_r/\delta = 0.9$. The white line marks the locus of points of maximum TKE found along the z-direction at each point in x. The location of maximum TKE can be considered as the approximate centre of the shear layer.

The qualitative organization of the mean shear layer can be described as follows: the shear layer appears to originate just downstream of the mean separation point, from where it grows in width until its growth is confined by the wall on the inclined side of the ramp. Its energy then smears out as it dissipates downstream of reattachment. The shear layer centre appears to form a straight line between a point near the wall just downstream of the shock foot to a point about 0.5δ above the mean reattachment. Downstream of reattachment, the line of maximum TKE runs essentially parallel to the ramp wall. This qualitative description is used to define a coordinate system for the developing portion of the shear layer. The axes of the shear layer coordinates are denoted by x' and z' where x' is oriented along the line of maximum TKE above the recirculating zone. The z'-axis is perpendicular to x' and pointed away from the wall. The origin of the mixing layer coordinates is the point at which the x'-axis intersects the wall upstream of the ramp. The distance of the shear layer coordinate's origin from the ramp corner is denoted by $x_{o1} = -1.90\delta$. The shear layer coordinates are included in Figure 2 and they make an angle of 16.5^o to the computational coordinates. This angle is comparable but slightly

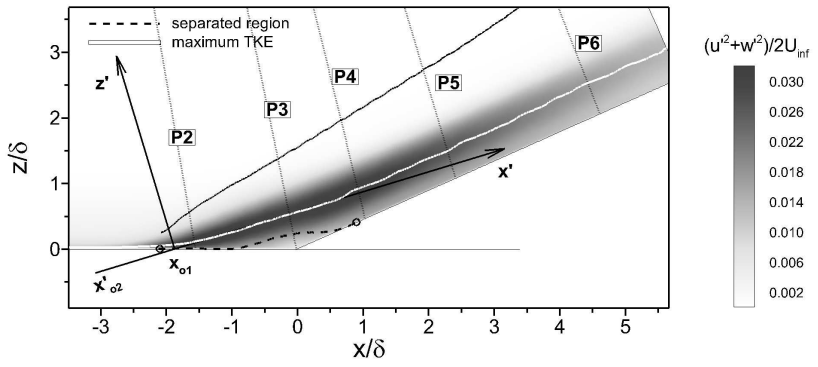

Figure 2: Spatial organization of the average shear layer. Contours of the time- and spanwise-averaged two-dimensional kinetic energy, $TKE = (u'^2 + w'^2)/2U_{\text{inf}}^2$. Time- and spanwise-averaged: shock location (solid black); approximate shear layer (white line); and dividing streamline for separated flow (dashed black).

higher than the shear layer angle of 11.5^o found by Dussauge, Piponniau, and Dupont [19] in the PIV data of reflected shock experiments at Mach 2.3 and $Re_\theta = 5100$ with flow deviation of 8.5^o and 9^o. Delery & Marvin [1] also state that a typical experimental value of the shear layer's inclination to the wall is on the order of 11^o.

If the shear layer does in fact grow linearly it should be possible to define a similarity variable, namely $\zeta = z'/(x' - x'_{\text{o2}})$, that will collapse the velocity profiles to a single similarity solution. The parameter x'_{o2} as indicated in Figure 2 is defined as the (imaginary) geometric origin of the shear layer and is found by varying the position of x'_{o2} along the x'-axis until what is deemed a good quality collapse of velocity profiles results. A value of $x'_{\text{o2}} = 1.41\delta$ was found to produce qualitatively the best collapse. In Figure 3 the profiles of the mean velocity and the two-dimensional Reynolds stresses $\overline{u'^2}$, and $\overline{u'w'}$ are plotted against the similarity variable ζ. Here the u' and w' indicate velocity fluctuations where the velocity components are in the direction of the x' and z' axes respectively. In Figure 3 the velocity terms are non-dimensionalized by $U_1 = 470(\text{m/s})$ which is the inviscid compression ramp solution for the freestream velocity behind a shock generated by a 24^o ramp at $M = 2.9$. The velocity U_1 is therefore an estimate of

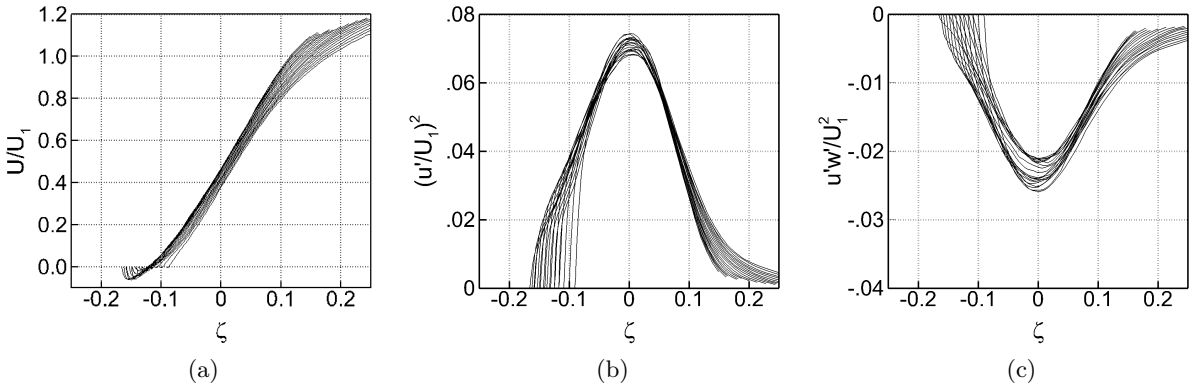

Figure 3: Collapse of profiles for (a) $\overline{U}$, (b) $\overline{u'^2}$, and (c) $\overline{u'w'}$ versus similarity variable ζ.

the freestream velocity on the shear layer's high-speed side. The profiles in Figure 3 are taken over the interval $-1.26\delta < x < 0.63\delta$. The streamwise and cross Reynolds stress profiles are well described as symmetrical about the mixing layer centre. In Figure 3, a spreading of the profiles on the low speed side is caused by the proximity of the wall surface. The profiles bear some resemblance to the profiles of a canonical mixing layer with self similarity as described by Townsend [20].

Dussauge *et al* [19] demonstrated with their experimental data of reflected STBLIs that is possible to estimate the spreading rate of the shear layer from the similarity profile of $\overline{u'^2}$. If it is assumed that the subsonic and supersonic mixing layers have the same $\overline{u'^2}$ profile shape, a comparison can be made between the widths of the two profiles and the compressible spreading rate can be determined from the incompressible spreading rate by the relation

$$\left(\frac{d\delta}{dx'}\right)_{\text{comp.}} = \frac{\zeta_{\text{comp.}}}{\zeta_{\text{incomp.}}}\left(\frac{d\delta}{dx'}\right)_{\text{incomp.}} \tag{1}$$

where $\zeta_{\text{incomp.}}$ and $\zeta_{\text{comp.}}$ are the widths of the two $\overline{u'^2}$ profiles at the same value of $\overline{u'^2}/max(\overline{u'^2})$. The spreading rate is denoted by $d\delta/dx$ where δ is the mixing layer thickness and is not to be confused with the boundary layer thickness from previous discussions. Using the subsonic mixing layer profiles of Mehta & Westphal [21], the linear spreading rate $d\delta/dx$ is estimated as 0.222. This result is comparable to the estimated spreading rates of 0.287 and 0.188 for 8^o and 9.5^o reflected shocks respectively by Dussauge *et al* [19].

4. Large-scale vortices – time and space organization

The velocity profiles of the time-averaged shear layer shown in Figure 3 are characterized by a low-velocity side and a high-velocity side connected by a single inflection point. The single inflection point in the mean velocity is associated with an inviscid instability that produces the large Kelvin–Helmholtz vortices visualized in planar mixing layers (For example see the visualizations by Mehta & Westphal [21]). Large, spanwise-oriented vortices shedding downstream of the interaction have been identified in the reflected shock experiments of Dupont, Piponniau, Sidorenko, and Debieve [15] and Souverein *et al* [13]. These vortices have also been identified in incompressible separation bubbles, for example in the experiments of Hillier & Cherry (1981) and Kiya & Sasaki [17, 23] and in the discrete vortex simulations of Kiya, Sasaki, and Arie [24]. In addition, Priebe & Martin [14] identified strong, streamwise-oriented vortices in the same DNS data we use in this analysis. It is apparent that the large vortices occurring in these separated flows are originating from the shear layer and are being generated by a similar mechanism as in the planar mixing layer, that is by the inviscid instability in the mean profile. The characteristic time and length scales of the large-scale vortices are described in this section.

4.1. Vortex characteristic time scale

Information on the average time period of the large vortices can be estimated from cross-correlations in time between signals of streamwise mass flux $(\rho u)'$ and the wall pressure P'_{w} if the following thought experiment is considered. The vortices are assumed to appear in the shear layer with more or less a regular spacing between them, with one being followed by the next. Any one of these large vortices in the shear layer will produce a negative fluctuation in the pressure at the wall surface just beneath the vortex core. It might also be reasonably assumed that in between successive vortices there is on average a positive fluctuation in the wall pressure. If a velocity signal is taken from a stationary point in the low-speed side of the shear layer, a negative fluctuation in velocity will occur in the signal when a vortex lies just above the 'probe' location and conversely a positive fluctuation would occur in between successive vortices. With this reasoning, a correlation between a mass flux signal at a point below the average mixing

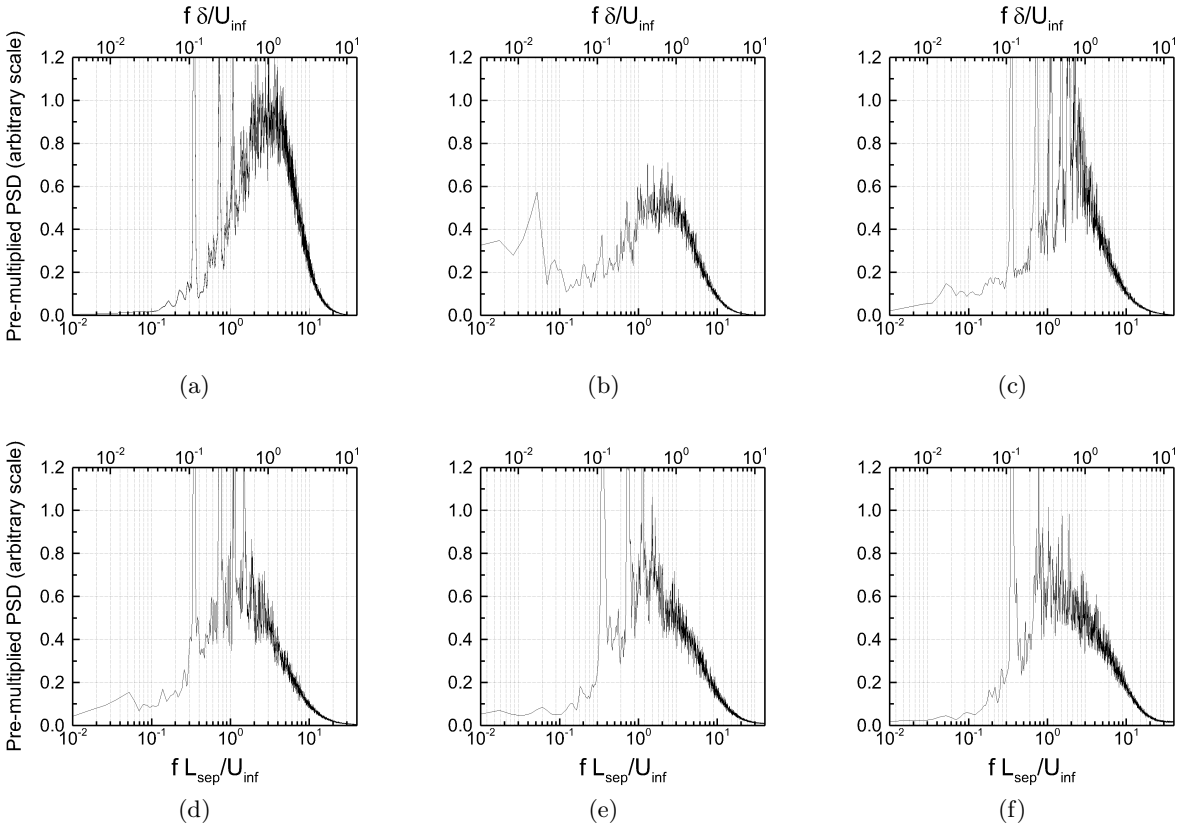

Figure 4: Pre-multiplied power spectrum plots for wall pressure signals at each of the grid planes indicated in Figure 1: (a)-(f) correspond to grid planes 1-6.

layer centre, and the signal of wall pressure just below that, should provide some information on the average periodic organization of the shear layer vortices. In fact, the auto-correlations of wall pressure by Hillier & Cherry [22] and the two-point correlations between velocity and wall pressure of Kiya & Sasaki [23] in incompressible separated shear layers show that these types of correlations produce a sinusoidal curve. The time period between successive vortices is the time period of the sinusoid. (See for example Figure 25 in Kiya & Sasaki [23].)

When performing two-point cross-correlations of the raw DNS time signals, both the smallest scales of the turbulence and the low-frequency motions of the shock tend to wash out the expected periodic shape of the mixing layer correlation curves. To retain only the signature of the large rollers, the data is first band-pass filtered before calculating the correlations. The band-pass filter is designed based on frequency information in the pre-multiplied power spectra of the wall-pressure signal. The pre-multiplied power spectral density (PSD) of the time signals of wall pressure at each of the high-frequency grid planes from Figure 1 are plotted in Figure 4. In Figure 4a, in the upstream boundary layer, a single broadband peak exists in the spectrum but, as the boundary layer passes through the interaction region (subsequent figures b-f), the centre of this peak undergoes a slight shift from a frequency $f \approx 5U_{\text{inf}}/L_{\text{sep}}$ to $f \approx 1U_{\text{inf}}/L_{\text{sep}}$. Just downstream of the shock at grid plane 2 shown in Figure 4b a second broadband energy peak appears at $f \approx 0.03U_{\text{inf}}/L_{\text{sep}}$. This second peak is associated with the low-frequency unsteadiness of the shock, and it is seen to disappear downstream of the separated region in Figures 4e and 4f. In addition to the broadband peaks, tall spikes are also apparent in the

Table 2: Summary of enhanced correlation results.

GridPlane	ΔT $(U_{\rm inf}/L_{\rm sep})$	f $(L_{\rm sep}/U_{\rm inf})$	$z_{\rm probe}$ (δ)	$\zeta_{\rm probe}$	$N_{\rm e}/N$
2	0.547	1.828	0.089	-0.009	40 / 3072
3	0.691	1.447	0.196	-0.104	236 / 2720
4	0.849	1.178	0.571	-0.065	584 / 2720
5	0.832	1.202	1.189	—	740 / 2720
6	0.834	1.214	2.176	—	865 / 2720

spectra of Figure 4. As explained by Priebe & Martin [14], these are associated with a forcing of the turbulence by the recycling inflow method used in the simulation of the auxiliary DNS, which is in turn used as the inlet condition of the ramp simulation. As it turns out, if the first harmonic ($f \approx 0.35U_{\rm inf}/L_{\rm sep}$) of the rescaling frequency is filtered from the data, the subsequent harmonics do not effect in any significant way the results of the cross-correlation analysis. In order to remove from the data the effects of (1) the low-frequency cycle energy, (2) the first harmonic of the forcing introduced by the inflow condition, and (3) the finest scales of the turbulence, a finite impulse response (FIR) band-pass filter was designed with high- and low-frequency cutoff values of $0.4U_{\rm inf}/L_{\rm sep}$ and $10.0U_{\rm inf}/L_{\rm sep}$.

The band-pass filtering alone was not sufficient to bring out the desired sinusoidal shape in the cross-correlations and so a conditional averaging technique was used in addition to the filtering to produce 'enhanced' correlations. The enhanced correlations were computed as follows: the time signals of mass flux and wall pressure at each of the grid planes labelled in Figure 1 were first band-pass filtered, broken up into shorter time segments, and then cross-correlations were calculated between each pair of corresponding shortened $(\rho u)'$ and $P'_{\rm w}$ time signals. If the short correlation had the desired sinusoidal shape, it was retained for averaging, and if no such large-scale pattern was detected the time segments were discarded. This is similar to the method of enhanced correlations between mass flux and wall-shear stress used by Brown & Thomas [25] in their studies of the coherent structures in turbulent boundary layers.

Correlations were computed at grid planes 2-6 where streamwise mass flux signals were taken

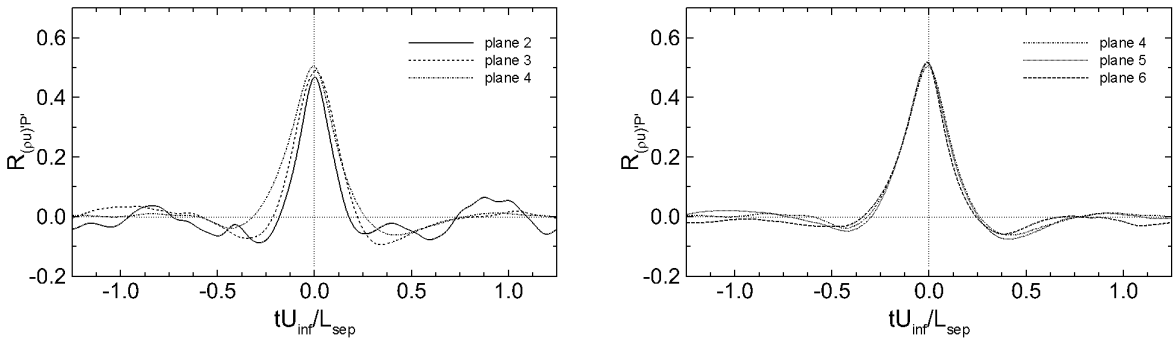

(a) (b)

Figure 5: Enhanced correlations $R_{(\rho {\rm u})'{\rm P}'}$ for (a) grid planes 2-4 and (b) 4-6.

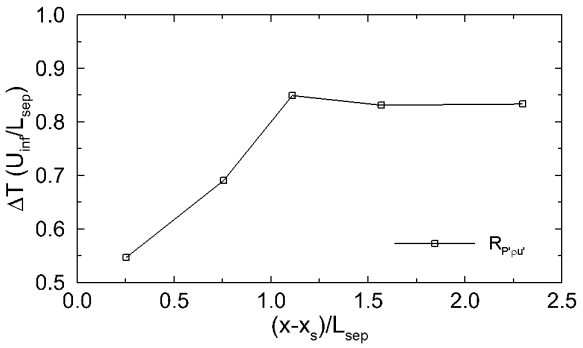

Figure 6: The time period ΔT between successive mixing-layer vortices versus downstream distance from the mean separation point x_{s}.

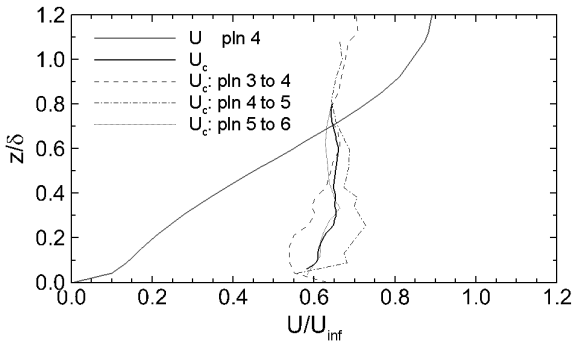

Figure 7: Average vortex convection velocity profile compared to the mean velocity profile at grid plane 4.

from 32 equally spaced points along the spanwise direction at a single wall-normal location. For grid planes 3-6 the time signals were broken up into $t = 5.8\delta/U_{\mathrm{inf}}$ long segments, approximately 2.5 times the period of the central frequency in the wall-pressure spectra. At grid plane 2 slightly shorter segments were used, as it was found that a time segment duration of $t = 5.0\delta/U_{\mathrm{inf}}$ produced stronger correlations at this plane. For a short correlation to be retained, two criteria had to be met. First, the cross-correlation curve at zero time lag must be greater than 0.4 (approximately twice the maximum of the non-enhanced correlations). Second, a minimum of less than -0.2 must occur at some point in the cross-correlation curve. The resulting enhanced correlations $R_{(\rho \mathrm{u})'\mathrm{P}'}$ are plotted in Figure 5. The average time period ΔT between vortices is estimated as the distance between the two minima of the correlation curves, and are summarized in Table 2. For each grid plane, the timescale, the corresponding shedding frequency, the wall-normal location of the mass flux signals, and also the number of segments retained for the enhanced correlations over the total number of segments tested (N_{e}/N) are given. It is worth mentioning that no such periodic pattern was found in the two-point correlations in the incoming boundary later at grid plane 1.

Two important observations are made from this analysis. First, if the time scales in Table 2 are plotted versus $(x - x_{\mathrm{s}})/L_{\mathrm{sep}}$ (see Figure 6), it is apparent that the time scale grows almost linearly through the separated region and then levels off to approximately a constant value downstream of reattachment. The same trend in the development of the time scale was observed by Kiya & Sasaki [23]. Second, the frequencies reported in Table 2 are located at the approximate centre of the broad-band peak in the pre-multiplied PSD plots of the wall pressure at each grid plane. Kiya and Sasa [23] also showed that the broad-band peak in their wall-pressure power spectrum at reattachment was centred at the average vortex shedding frequency.

4.2. Vortex convection velocity

The frequency reported for grid plane 4 in Table 2 is interpreted as the shedding frequency of the large-scale vortices from the separated region of the interaction. It is assumed that these vortices propagate downstream of reattachment at approximately a constant convection velocity, as would be consistent with the levelling off of the vortex time scale observed in Figure 6. The convection velocity of the vortices can be estimated from two-point correlations calculated between mass-flux signals separated by some known distance in the streamwise direction. The average time it takes for an eddy to convect from the first signal location to the second is given by the offset of the peak in the cross-correlation curve. Thus it follows that the eddy convection velocity is this time lag divided by the distance between the two probes.

The two-point correlations are calculated between streamwise mass flux signals from adjacent high-frequency output planes. In this analysis, streamwise mass fluctuations $(\rho u)'$ now refer to fluctuations in the direction of the local mean streamline. Also, correlated signals between adjacent grid planes are chosen so that they lie on the same mean streamline. To determine an average convection velocity of the large vortices specifically, the time signals are filtered using a narrow band-pass FIR filter designed to retain frequencies between $f = 0.4U_{\rm inf}/L_{\rm sep}$ and $2.0U_{\rm inf}/L_{\rm sep}$, or roughly half to twice the average shedding frequency. Three separate estimates of convection velocity profiles were computed from correlations between grid planes 3 and 4, between grid planes 4 and 5, and between grid planes 5 and 6. The convection velocity profiles and the mean velocity profile at grid plane 4 are plotted together in Figure 7. A final value for the convection velocity is estimated by an average over the three resulting velocity profiles, or $U_{\rm c} = 0.65U_{\rm inf}$, where $U_{\rm c}$ is in the direction parallel to the ramp surface.

4.3. Vortex spatial organization

The convection velocity $0.65U_{\rm inf}$ multiplied by the vortex timescale of $0.85L_{\rm sep}/U_{\rm inf}$ at grid plane 4 yields an average spacing of $0.55L_{\rm sep}$ or 1.7δ between vortices downstream of reattachment. In their reflected shock experiments, Dupont *et al* [15] reported a spacing of approximately $0.4L_{\rm sep}$.

Additional qualitative information on the average spatial organization of the mixing layer vortices can also be observed from the two-dimensional (2D) correlations defined by

$$R_{(\rho {\rm u})'{\rm P}'} = \frac{\langle (\rho u)'(x+\Delta x, y+\Delta y, z) P'(x,y)\rangle}{\langle (\rho u)'_{\rm rms} P'_{\rm rms}\rangle}. \qquad (2)$$

The 2D correlations are calculated from the time signals at grid plane 4, where x is substituted with the quantity $tU_{\rm c}$. The resulting correlation plots therefore describe vortex structures that are essentially frozen in space as they convect past grid plane 4. Before computing the

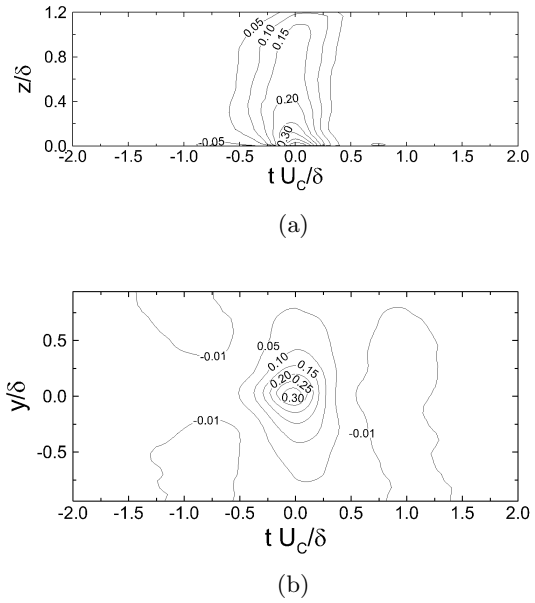

Figure 8: Contour plots of 2D correlations $R_{(\rho {\rm u})',{\rm P}'}$ (a) in the xz-plane at $y/\delta = 0$ and (b) in the xy-plane at $z/\delta = 0.1$.

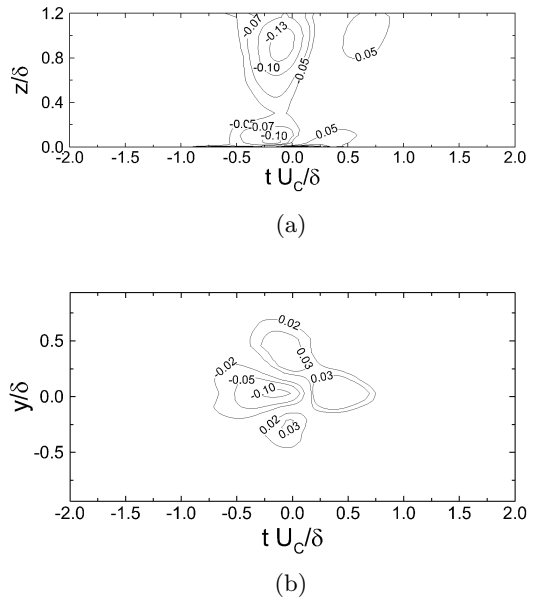

Figure 9: Contour plots of 2D correlations $R_{(\rho {\rm w})',{\rm P}'}$ (a) in the xz-plane at $y/\delta = 0$ and (b) in the xy-plane at $z/\delta = 0.1$.

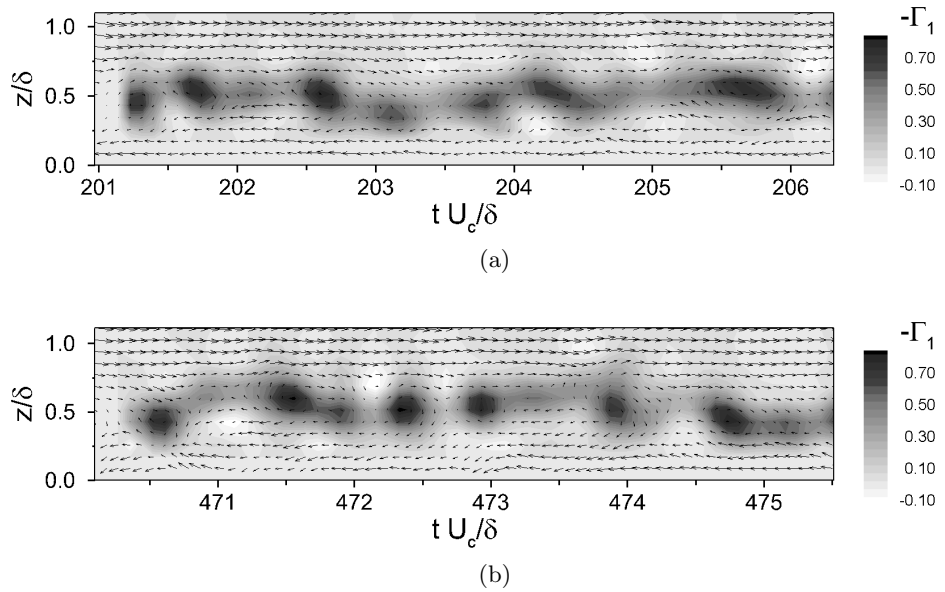

Figure 10: Contour plots of the vortex detector Γ_1 for two separate snapshots in time at grid plane 4. A value of $|\Gamma_1| > 0.63$ represents a vortex core.

correlations, the time signals of mass flux and wall pressure are band-pass filtered in time with a new filter that retains frequencies between $0.4U_{\rm inf}/L_{\rm sep}$ and $5.0U_{\rm inf}/L_{\rm sep}$. The same signature pattern of the large vortices is observed in the correlation plots, regardless of whether the high-frequency cutoff is set to $10.0U_{\rm inf}/L_{\rm sep}$ as in section 4.1, or to $5U_{\rm inf}/L_{\rm sep}$. However, the pattern is a bit more prominent when the high-frequency cutoff is set to $5.0U_{\rm inf}/L_{\rm sep}$. Contour plots of the 2D correlations between $(\rho u)'$ and $P'_{\rm w}$ are shown in Figure 8. In Figure 8a is plotted $R_{(\rho {\rm u})',{\rm P}'}$ in the xz-plane at $y = 0$ and in Figure 8b is plotted $R_{(\rho {\rm u})',{\rm P}'}$ in the xy-plane of $z = 0.1\delta$. If Taylor's hypothesis of frozen turbulence is assumed true for the large vortices, positive $tU_{\rm c}/\delta$ in Figure 8 would correspond to structures downstream of plane 4, and negative $tU_{\rm c}/\delta$ to structures upstream of plane 4. A large-scale structure is observed that extends in the wall-normal direction across the entire boundary layer. The 'footprint' for this structure is approximately 2δ in streamwise length. It is at once obvious that the large shear-layer vortices are three-dimensional in nature, since there appears to be an angle or kink in the structure pattern (see the xy-plane correlation plot shown in Figure 8b). This asymmetry is even more apparent in the 2D correlations between wall-normal mass flux and wall-pressure $R_{(\rho {\rm w})'{\rm P}'}$ that are plotted in Figure 9 for the same planes. In Figure 9b, an angle of about 45^o to the x-axis is seen in the region of positive correlation.

The $R_{(\rho {\rm w})'{\rm P}'}$ correlations can be interpreted using the same arguments as those that were used in section 4.1. When a vortex exists just above a probe located in the low-speed side of the mixing layer, the wall-normal velocity will on average have a zero fluctuation. If the vortex is just ahead or behind the probe a negative or positive fluctuation respectively might be expected to occur. In addition, in between vortices, there is zero fluctuation in wall-normal velocity. As a result, the fluctuations in wall-normal velocity follow the same pattern as the fluctuations in wall pressure, only shifted ahead in time by a fourth of the time period of the vortices. Returning to Figure 9b, there is a positive lobe in the 2D correlations that is centred at approximately $tU_{\rm c}/\delta = 0.4$, or about a fourth of the average vortex spacing of 1.7δ derived earlier, and a lobe of negative correlations just to the left of $tU_{\rm c}/\delta = 0$. The results suggest that the vortices are

angled in the xy-plane instead of spanning the width of the domain in a straight line.

An effort is made to explain the structure appearing in the 2D correlations of Figures 8 and 9 by visualizing individual (frozen) vortices in the time data of grid plane 4. A number of methods exist for the identification and visualization of vortical structures in turbulent flows. The goal here is to pick out specifically the large-scale vortices whose vortex cores are oriented in the spanwise direction in order to keep the pictures clear and not cluttered, for example by streamwise oriented vortices. Although it is a rather crude method for the identification of vortices and is generally used for post-processing coarser PIV vector field data (for example see Dupont *et al* [15]), the 2D vortex identification criteria Γ_1 of Graftieaux, Michard, and Grosjean [26] is used here primarily because of its simple and robust formulation. If P is a point in a 2D vector field, S is some area surrounding P, and M is a point inside S, the vortex detector Γ_1 is defined by

$$\Gamma_1(P) = \frac{1}{S}\int_{M\in S} \frac{(\mathbf{PM}\times\mathbf{U}_\mathrm{M})\cdot\mathbf{z}}{|\mathbf{PM}|\cdot|\mathbf{U}_\mathrm{M}|}dS = \frac{1}{S}\int_S \sin\theta_\mathrm{M} dS \tag{3}$$

where $\mathbf{PM}$ is the vector connecting points P and M, $\mathbf{U}_\mathrm{M}$ is the velocity vector at point M and θ_M is the angle between vectors $\mathbf{PM}$ and $\mathbf{U}_\mathrm{M}$. The parameter Γ_1 will be between -1 and 1 depending on the direction of rotation and it can be shown that a vortex exists when $|\Gamma_1| > 2/\pi$. For a rectangular interrogation area with N discrete points inside that area, equation 3 can be re-expressed as

$$\Gamma_1(P) = \frac{1}{S}\int_S \sin\theta_\mathrm{M} dS = \frac{1}{N}\sum_N \sin\theta_\mathrm{M} \tag{4}$$

The vector field is generated from time signals of u and w at grid plane 4 filtered using the same filter as for the 2D correlations, and then converted to space in the streamwise direction using again the variable $tU_\mathrm{c}/\delta \approx x/\delta$. The constant convection velocity $U_\mathrm{c} = 0.65U_\mathrm{inf}$ is subtracted from u and the velocity vectors are weighted by the local mean density ratio $\overline{\rho}(z)/\overline{\rho}_\mathrm{w}$ to account for compressibility effects across the shear layer in the form of a Morkovin-type density scaling [27]. Using a square interrogation area of size $0.15\delta^2$, the vortex detector Γ_1 is computed using equation (4) on the density-weighted, convecting velocity vector field in the xy-plane taken from the spanwise centre of grid plane 4. Two separate segments in time of the vector field and the corresponding contour plot of Γ_1 are plotted in Figure 10 to demonstrate typical results from the vortex detection method. The large vortices are visualized by the dark areas, which appear predominantly at the wall-normal distance of 0.5δ. This result is consistent with the location of the shear-layer centre at grid plane 4, shown in Figure 2. The individual vortices seem to be spaced apart by 0.5 to 2δ.

If Γ_1 is calculated at every xz-plane across the span of grid plane 4, a three-dimensional representation of the vortices can be constructed. The 3D isosurfaces of $\Gamma_1 = -2/\pi$ at the same time segments as in Figure 10 are plotted in Figures 11 and 12. From these images the individual vortices look to be about 0.5 to 1δ long, and almost all of the vortices are at an angle of approximately 45^o to the flow. In fact, a number of these vortices are bent in the centre forming an arrowhead shape. This behaviour explains the structure angle seen in the 2D correlation plots of Figures 8b and 9b. From Figures 11 and 12 the direction of the angle is equally possible for forming arrows pointed upstream as for arrows pointed downstream. However, the 2D contour plots appear to be biased towards the upstream pointed vortices. The vortex cores also seem to be more or less confined to the xy-plane at $z/\delta \approx 0.5$.

5. Conclusions

In this paper a thorough characterization of the time-averaged organization of the shear layer in a Mach 3 STBLI over a 24^o compression ramp is presented. This analysis consisted of defining

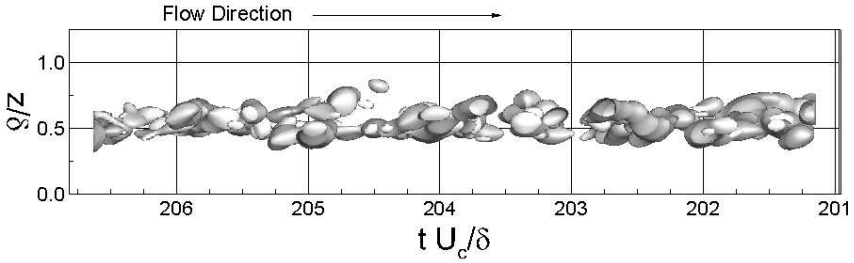

(a)

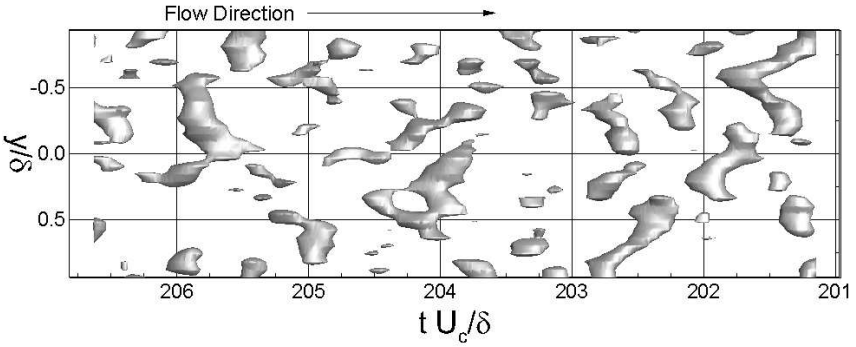

(b)

Figure 11: Vortex structure visualized the isosurface of $\Gamma_1 = -2/\pi$ at 'snapshot 1'.

the time- and spanwise-averaged position of the shear layer. Specifically, it was shown that the shear layer centre forms a straight line between the origin at the wall just downstream of the shock and a point just above the mean reattachment point. The angle between the shear layer and the wall is found to be 16.5^o. In addition, it was shown that, above the separated region, the shear layer grows approximately linearly up to the mean reattachment point. If a coordinate system is defined where the x-axis is pointed along the centre of the shear layer, a similarity variable can be defined. The similarity variable collapses the profiles of mean velocity and 2D Reynolds stresses to a single similarity profile. The linear spreading rate is determined from the profiles. This same analysis was first done by Dussauge, Piponniau, and Dupont [19] using their reflected shock PIV data and the current results are comparable to those from the reflected shock.

In addition to the time-averaged definition of the shear layer orientation, the frequency content of the shear layer is also analysed. Time and length scales of the large-scale vortices produced by the shear layer are estimated, as well as the average convection velocity of these vortices. It is shown that the time period between successive vortices increases almost linearly through the developing region of the shear layer and then becomes constant downstream of reattachment. It is apparent that the spreading of the shear layer is caused by the growth of the large-scale vortices that increase in size until they are confined by the surface of the ramp. The point of reattachment of the flow might therefore be dependent on the growth rate of the shear layer and also the angle the shear layer makes to the wall surface. In addition, the development of the average vortex timescale is consistent with the shift in frequencies that are seen in the pre-multiplied power spectra of the wall pressure.

Contour plots of correlations between mass flux and wall pressure resulted in a wall signature

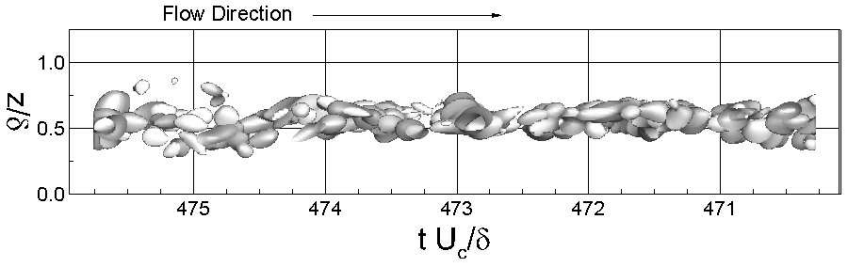

(a)

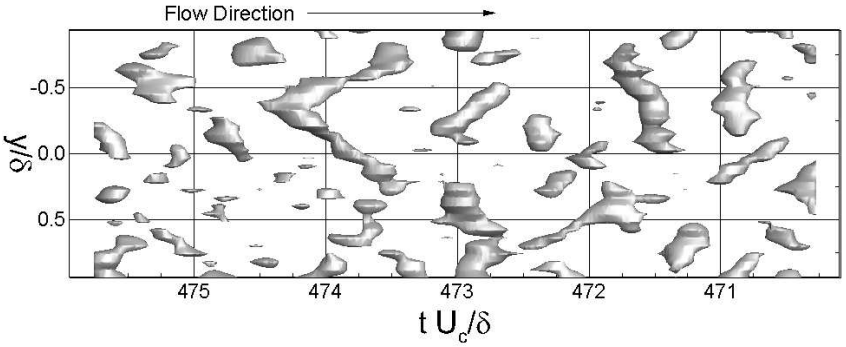

(b)

Figure 12: Vortex structure visualized the isosurface of $\Gamma_1 = -2/\pi$ at 'snapshot 2'.

that suggests the shear layer vortices are not two-dimensional in nature. The visualization of individual vortices using the vector detector of Graftieaux *et al* [26] provides proof that this is in fact the case. The vortex cores just downstream of reattachment are found to generally remain in a plane parallel to the wall surface, and are angled in either direction approximately 45^o from the direction of the freestream. The shear layer shows resemblance to a canonical mixing layer in xyz. A distinct difference is that, in the STBLI case, the shear layer structures make the observed 45^o angle with the flow, showing a crisscrossing pattern on streamwise-spanwise planes.

Acknowledgments

This work is supported by the Air Force Office of Scientific Research under grant AF/9550-10-1-0164, and in part by the Multiflow Program of the European Research Council at the Universidad Politécnica de Madrid (Spain).

References

[1] Delery J and Marvin J G 1986 Shock-Wave Boundary Layer interactions *AGARDograph* **280** (Paris: NATO)
[2] Dolling D S 2001 Fifty Years of Shock-Wave/Boundary-Layer Interaction Research: What Next? *AIAA J.* **39** 1517–31
[3] Smits A J and Dussauge J P 2006 *Turbulent Shear Layers in Supersonic Flow* (New York: Springer)
[4] Clemens N T and Narayanaswamy V 2009 Shock/Turbulent Boundary Layer Interactions: Review of Recent Work on Sources of Unsteadiness *AIAA Paper* 2009-3710
[5] Beresh S J, Clemens N T and Dolling D S 2002 Relationship Between Upstream Turbulent Boundary-Layer Velocity Fluctuations and Separation Shock Unsteadiness *AIAA J.* **40** 2412–22
[6] Dupont J, Haddad C and Debieve J-F 2006 Space and time organization in a shock-induced separated boundary layer *J. of Fluid Mech.* **559** 255–77

[7] Ganapathisubramani B, Clemens N T and Dolling 2007 Effects of upstream boundary layer on the unsteadiness of shock-induced separation *J. Fluid Mech.* **585** 369–94
[8] Robinet J Ch 2007 Bifurcations in shock-wave/laminar-boundary-layer interaction: global instability approach *J. Fluid Mech.* **579** 85–112
[9] Wu M and Martin M P 2008 Analysis of shock motion in shockwave and turbulent boundary layer interaction using direct numerical simulation data *J. Fluid Mech.* **594** 71–83
[10] Piponniau S, Dussauge J-P, Debieve J-F and Dupont P 2009 A simple model for low-frequency unsteadiness in shock-induced separation *J. Fluid Mech.* **629** 87–108
[11] Ganapathisubramani B, Clemens N T and Dolling 2009 Low-frequency dynamics of shock-induced separation in a compression ramp interaction *J. Fluid Mech.* **636** 397–425
[12] Humble R A, Scarano F, van Oudheusden B W 2009 Unsteady aspects of an incident shock wave/turbulent boundary layer interaction *J. Fluid Mech.* **635** 47–74
[13] Souverein L J, Dupont P, Debieve J-F, Dussauge J-P, van Oudheusden B and Scarano F 2010 Effect of interaction strength on unsteadiness in turbulent shock-wave-induced separations *AIAA J.* **48** 1480–93
[14] Priebe S and Martin MP 2012 Low-frequency unsteadiness in shock waveturbulent boundary layer interaction *J. Fluid Mech.* **699** 1–49
[15] Dupont P, Piponniau S, Sidorenko A and Debieve J-F 2008 Investigation by Particle image velocimetry measurements of oblique shock reflection with separation *AIAA J.* **46** 1365–70
[16] Agostini L, Larchevêque L, Dupont P, Debiève J-F and Dussauge J-P 2012 Zones of influence and shock motion in a shock/boundary-layer interaction *AIAA J.* **50** 1377–87
[17] Kiya M and Sasaki K 1985 Structure of large-scale vortices and unsteady reverse flow in the reattaching zone of a turbulent separation bubble *J. Fluid Mech.* **154** 463–91
[18] Xu S and Martin M P 2004 Assessment of inflow boundary conditions for compressible turbulent boundary layers *Phy. of Fluids* **16** 2623–39
[19] Dussauge J-P, Piponniau S and Dupont P 2010 *APS 63rd Annual DFD Meeting, Long Beach, CA*
[20] Townsend A A 1976 *Structure of Turbulent Shear Flow* (Cambridge: Cambridge Univ. Press)
[21] Mehta R D and Westphal R V 1984 Near-field turbulence properties of single- and two-stream plane mixing layers *AIAA Paper* 84-0426
[22] Hillier R and Cherry N J 1981 The effects of stream turbulence on separation bubbles *J. of Wind Eng. Ind. Aerodynamics* **8** 49–58
[23] Kiya M and Sasaki K 1983 Structure of a turbulent separation bubble *J. Fluid Mech.* **137** 83–113
[24] Kiya M, Sasaki K, and Arie M 1982 Discrete-vortex simulation of a turbulent separation bubble *J. Fluid Mech.* **120** 219–44
[25] Brown G L and Thomas A S W 1977 Large structure in a turbulent boundary layer *Phys. of Fluids* **20** S243–52
[26] Graftieaux L, Michard M and Grosjean N 2001 Combining PIV, POD and vortex identification algorithms for the study of unsteady turbulent swirling flows *Meas. Sci. Tech.* **12** 1422–9
[27] Morkovin M V 1962 *Mécanique de la Turbulence* (Paris: CNRS)